



# Smart laser osteotomy: integrating a pulsed 1064nm fiber laser into the sample arm of a fiber optic 1310nm OCT system for ablation monitoring

JAMIL JIVRAJ,<sup>1</sup> CHAOLIANG CHEN,<sup>1</sup> YIZE HUANG,<sup>1</sup> JOEL RAMJIST,<sup>1</sup> YI LU,<sup>2</sup> BARRY VUONG,<sup>1</sup> XIJIA GU,<sup>2</sup> AND VICTOR X. D. YANG<sup>1,3,4,\*</sup>

<sup>1</sup>Biophotonics and Bioengineering Lab, Department of Electrical and Computer Engineering, Ryerson University, Toronto, Canada

<sup>2</sup>Fiber Optics Communications and Sensing Lab, Department of Electrical and Computer Engineering, Ryerson University, Toronto, Canada

<sup>3</sup>Division of Neurosurgery, Sunnybrook Health Sciences Centre, Toronto, Canada

<sup>4</sup>Department of Surgery, Faculty of Medicine, University of Toronto, Canada

\*yangv@ee.ryerson.ca

**Abstract:** Real-time depth metrology during material removal via laser ablation is useful in many forms of laser machining. Until now, coaxial optical coherence tomography (OCT) metrology was achieved by the coupling of an OCT imaging beam and ablating beams using a dichroic filter. We present an alternative design with all fiber delivery that is more suitable for surgical laser ablation applications. The novel system design integrates a high peak-power pulsed Yb-doped fiber laser (1064nm) coupled directly into the sample arm of a swept-source OCT system ( $\lambda_c = 1310\text{nm}$ ). We measured the OCT signal degradation due to dispersion and attenuation through the ablation fiber laser cavity. Ablation progression is measured in real-time using M-mode OCT. The mean depth targeting error was found to range from  $10\mu\text{m}$  to  $80\mu\text{m}$  in phantom ablation experiments and  $21\mu\text{m}$  to  $60\mu\text{m}$  in bone ablation. A number of issues have been solved, including point-spread function (PSF) peak broadening due to signal delay and dispersion, high bending loss due to dissimilar fiber used throughout the design, and problems due to the extremely high ablation power to swept-source power ratio ( $> 2 \times 10^4$  peak to average power). To our knowledge, this is the first demonstration of thermal-mediated laser ablation drilling integrated with coaxial OCT imaging through a single-mode, single-cladded output fiber, without using dichroic beam splitters or free-space optic filters anywhere in the optical path and with this high ablation laser power to OCT source power ratio. The removal of bulk optics compared to existing designs opens a new path for compact integration of the entire system. Also, since the ablation laser and OCT feedback system exist along the same fiber path, the need for maintenance and repair are greatly reduced since spatial beam alignment and the potential open-air contamination of optical surfaces are virtually eliminated. We believe that this integrated system is a great candidate for adoption in depth-controlled surgical ablation applications.

© 2018 Optical Society of America under the terms of the [OSA Open Access Publishing Agreement](#)

## 1. Introduction

Having the capability of visualizing and quantifying material morphology change during laser material processing can be useful to control quality and efficacy of cutting and/or ablation. However, these parameters are controlled based on post irradiation analysis of the end result, which leads to an iterative trial-and-error process. This does not allow for real-time parameter adjustment and optimization during ablation. As well, controlled depth of material removal is based solely on experience and a priori knowledge of interaction dynamics between the material and the specific characteristics of the laser beam [1]. This becomes significantly less reliable when

dealing with biological tissue, assumptions have to be made about homogeneity [2,3]. Because of this, having the ablation front approach material boundaries with high precision and close proximity without full breach becomes a very difficult task. Cameras with high magnification optics have been used [4], but this approach has inherent disadvantages. Optimal viewing angle must be decided prior to ablation. In addition, a camera system cannot visualize sub-surface ablation activity. A distinct advantage of OCT in visualizing the ablation process is that the imaging beam can travel coaxially with the ablation beam; even using the same focusing optics. This allows for high resolution, sub-surface imaging (limited to imaging depth of OCT) right at and in proximity of the site of ablation activity.

Boppart *et al* [5] were the first to report real-time ablation monitoring of tissue using OCT. Rat organs were ablated using a continuous wave (CW) argon laser at 514nm. B-mode OCT visualization of the process was captured at approximately 8 frames per second. Coaxial beam coupling was achieved with a dichroic mirror. The results clearly show formation of ablation crater and subsequent formation of carbonized and possibly hyperthermic tissue along the crater boundary, consistent with thermal-dominant tissue ablation. A second study done by the same group [6] showed the feasibility of using OCT to monitor soft tissue ablation during transurethral resection of prostate (TURP) surgery using an argon laser. Ohmi *et al* [7] demonstrated inline OCT monitoring of in-situ ablation of a human tooth using a Q-switched Nd:YAG laser at 1.06  $\mu\text{m}$  with a 10ns pulse width. The OCT and ablation laser were time-multiplexed across a dichroic mirror using an electronic shutter. A certain number of pulses were fired onto the tooth, at which point the shutter was closed to block the ablation laser, and the OCT system was allowed to take a B-mode image. This process was repeated until the crater reached various depths. A study by Oh *et al* [8] achieved high-speed imaging of ablation using a swept-source OCT (SS-OCT) with an A-line rate of 115kHz and a video rate of 200fps. Similar studies were done using FD-OCT systems combined with Nd:YAG and YAG lasers achieving 25 frame/s acquisition speeds [9, 10]. Torkian *et. al.* compared results of ablation crater metrics (width and depth) of porcine vocal cords between OCT and histology; no significant differences were found, thus proving OCT as a viable method of ablation depth measurement [11]. Although the authors of this study did not monitor ablation depth in real-time, the results prove that OCT is not only effecting in qualitative visualization of crater formation but is a viable tool to gather quantitative ablation related data – exactly what is needed to provide feedback in a closed loop controller. The first study showing in-situ, real time depth profiling during ablation was done by Webster *et. al.* [12]. The system described in the study used a single laser source for both ablation and imaging. A 1064nm mode-locked fiber laser with repetition rate of 10MHz and pulse duration of 20ps was expanded, then split using a Michelson interferometer into reference and sample beams. The sample beam was reflected off of a galvanometer-mounted mirror (used for beam positioning) and through a focusing objective lens. The light that was backscattered from the ablation process was combined with the reference beam at the interferometer and collected at the detection arm, where it was sent to a spectrometer. This study was able to demonstrate etch progression during ablation of stainless steel using M-mode OCT imaging (capturing OCT interferometric data at a single point rather than raster scanning the beam). The images generated were able to show when the ablation process sped up or slowed down. The A-line rate of the OCT system was 46kHz, despite the source's 10MHz pulse repetition rate. A similar studies by the same group demonstrated full control using OCT-based metrology as the feedback mechanism [13]. Demonstration of successful OCT feedback used during hard tissue ablation was demonstrated in [14]. The authors were able to control the percussion drilling to within 50 $\mu\text{m}$  of full breach of cortical bone, thereby proving the potential of OCT in controlling laser ablation for surgical applications.

Similar work using all-fiber designs have been carried out by Beaudette *et al.* [15, 16]. In both these studies, a coagulation laser was coupled to an OCT imaging system using a double-cladded fiber coupler, achieving essentially single-fiber beam delivery for coagulation and monitoring.

The power scalability for this method is limited for two primary reasons: first, fiber couplers tend to have a low damage threshold (typically in the hundreds of milliwatts). According to Boulnois [17], ablation in the thermal regime during laser-tissue interaction roughly begins at a power density of  $10 \text{ W/cm}^2$  with an exposure time of roughly  $10^{-3} \text{ s}$ ; plasma mediated ablation requires higher powers at smaller exposure times. This demonstrates the need for coupling of higher power sources with OCT for effective etching of bone in a controlled manner. Second, the OCT system is left vulnerable to damage from the higher power coagulation light source. As well, in [15], a required beam-dump at port 4 of the coupler reduces overall efficiency of the entire system.

In a 2015 study [18], we presented a precursor of this work where the integration of a 1kW peak power/10W average power fiber laser and swept-source OCT system was achieved using a series of edge-pass, free space filters. M-mode progression of wood ablation was shown for up to 2mm in ablation depth. This paper demonstrated the first time two laser systems of such high power difference were coupled into a single delivery fiber for use in an ablation-monitoring application. In 2017, a continuation of this work demonstrated a phenomenon where the peaks of the PSF were shown to broaden as a function of optical path difference [19].

In this paper, we present an integrated high peak-power 1064nm fiber laser within the sample arm of an OCT system at 1310nm center wavelength. This configuration allows for coaxial beam delivery without the use of a dichroic mirror at the output stage or any other free-space bulk optic elements for use in coupling. We also address and resolve the issue of depth-dependant PSF peak broadening.

## 2. Methods

Our goal was to develop a system that could ablate tissue and metrologically monitor the depth progression of ablation, without losing advantage of the flexibility of fiber optic delivery. Fig. 1 shows a schematic of the integrated system.

### 2.1. Construction of fiber laser

The 1064nm ablation laser light is produced by a high power fiber laser based on a design from [20]. It consists of an all-fiber active cavity approximately 10m in length, constructed of Yb-doped fiber (Nufern LMA-YDF-10/130-VIII). Two fiber Bragg gratings etched onto matching passive fiber (Nufern SM-GDF-10/125) are spliced onto the ends of the cavity, with an APC connector terminating the output end. The cavity is pumped using a 976nm fiber coupled laser diode (RealLight M976 $\pm$ 3-110-F105/22-D1) via a (2+1)x1 high power fiber combiner (ITF MM021112CC1A). It is important to note that all the fiber used in the construction of the fiber laser has a core diameter of  $10\mu\text{m}$ ; this means that the output beam can be focused down to a diffraction limited spot size since the output beam remains in single-mode. The characteristics of the fiber laser are summarized in Table 1.

Table 1. Parameters of fiber laser.

Wavelength	1064nm
Average Power	3.35W
Peak Power	419W
Pulse Duration	160ns
Pulse Frequency	50kHz

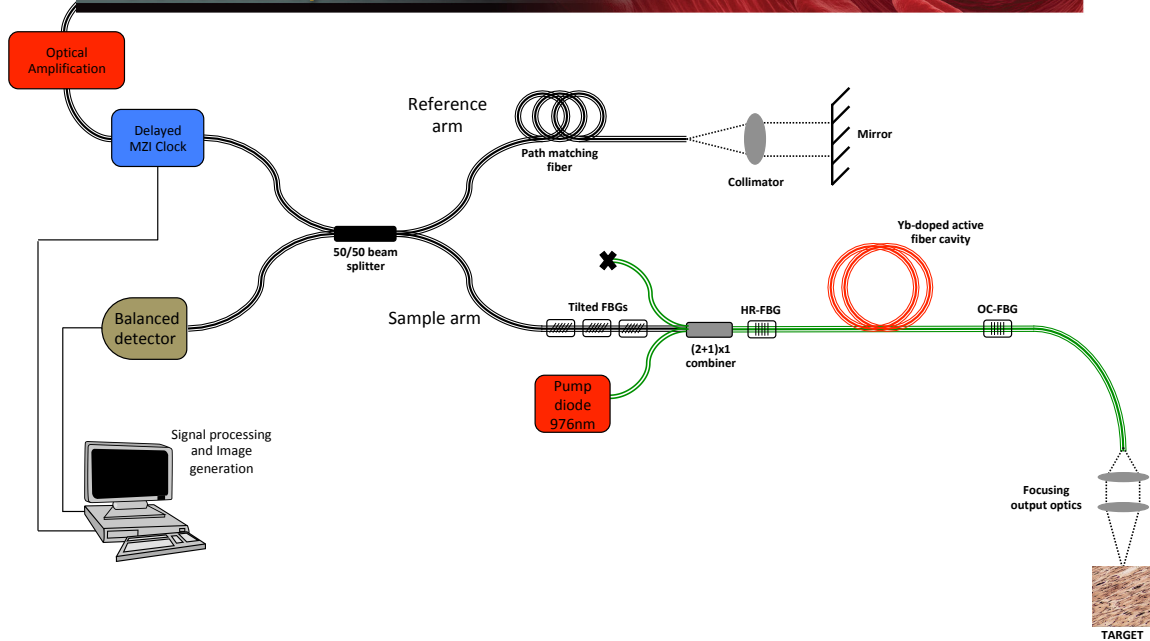


Fig. 1. Schematic of the integrated OCT and fiber laser system. The entire fiber laser is built directly into the sample arm of the OCT system. Both systems are entirely fiber-based (aside from standard reference arm and focusing optics), allowing compact, robust packaging and elimination of dual-beam free-space alignment.

## 2.2. Swept-source OCT

The OCT system consisted of a 1310nm centered swept wavelength MEMS laser (Santec HSL-20-50-S) with a bandwidth of 110nm, sweep rate of 50kHz (single-sided sweep, 62 percent duty cycle) and (measured) average power output of 18.5mW. An integrated Michaelson interferometer (50/50 coupling ratio) and balanced detector system was used. The entire OCT system was constructed using SMF-28 fiber. The MEMS laser provides a k-clock output for sampling trigger.

## 2.3. Coaxial sample arm coupling

Two important factors needed to be taken into consideration when assimilating the fiber laser into the sample arm of the OCT system. First, the path length of the sample arm needed to be matched in the reference arm to ensure interference can be detected; this was done by splicing an equivalent length of SMF-28 fiber into the reference arm of the OCT system. Second, there was a significant challenge in coupling the two sources since the ablation source had a peak power approximately 4 orders of magnitude higher than the average power of the OCT swept-source. This meant that any 1064nm laser light coming from the fiber laser, out of the power combiner towards the OCT system needed to be attenuated so that the balanced detector and any low damage threshold optics associated with the OCT system would not be destroyed. This was done by coupling both systems via three in-house made titled fiber Bragg gratings in series giving a total of 20dB attenuation of the 1064nm light.

### 2.3.1. Bending loss and amplification

It was found that the 1310nm centered swept-source light was being highly attenuated through the fiber laser-based sample arm. After accounting for splice loss and attenuation through in-line passive components, it was determined that the OCT light was subject to higher losses due to fiber bending. Upon further investigation, it was determined that bending of the SMF-28 fiber sections did not contribute much to the attenuation, and that most of the loss was attributed to bending of the large mode area (LMA) fiber sections. The SM-GDF-10/125 fiber has a numerical

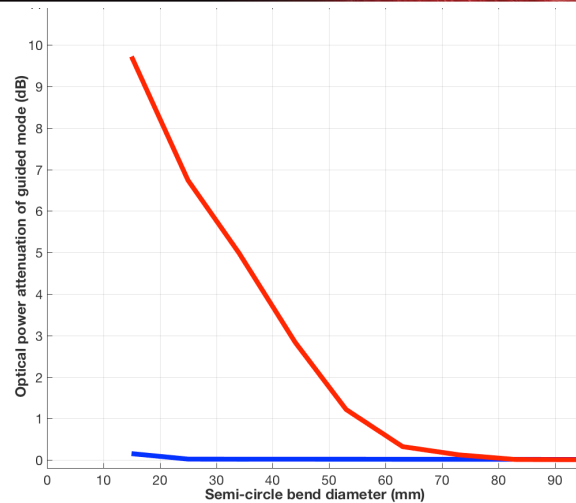


Fig. 2. OCT swept source light ejection from fiber core due to bending. For the data shown in this figure bends of 10 different diameters were performed, repeated three times and averaged. The red line represents the Nufern SM-GDF-10/125, and the blue line represents standard SMF-28 fiber. It is important to note how dramatic the ejection from the core of the Nufern SM-GDF-10/125 fiber is, up to approximately 53mm of bending diameter, compared to SMF-28.

aperture (NA) of 0.086, which is much lower than that of the SMF-28 [13]. Bending of the SM-GDF-10/125 allowed light guided in the core to leak into the cladding and the subsequent propagating through the cladding mode pump stripper was responsible for ejecting any light inside the cladding. It was found that at a 15mm bending diameter, the SM-GDF-10/125 fiber exhibited an 9.7dB attenuation of the OCT swept-source light; SMF-28 exhibited 0.15dB under the same radius. Bending loss of the 1310nm-centered broad band light is summarized in Fig. 2, where each fiber was bent in a semi-circle with varying diameters.

To increase the OCT light power through the sample arm, an optical amplifier (Covega BOA1017) was placed between the swept-source and interferometer, which increased the input power to 85mW. This brought the power out of OCT laser light at the output pigtail of the fiber laser to 6.5mW. The measured power loss after the ablation laser is approximately 8.15dB resulting in a total theoretical sensitivity of 81.7db sensitivity; the measured sensitivity was 80dB. The expected sensitivity was measured to be 98dB measured without ablation fiber in sample arm. This high attenuation is a principle limitation of this scheme; however the sensitivity of the system is more than adequate to provide clear surface detection. Strategies for mitigating further power lose due to output fiber bending are discussed in the Discussion section. In the context of ANSI safety standards, if we assume that the 6.5mW incident OCT light power (1310nm) is delivered at a 50% duty cycle of the 50KHz A-line rate, this approximates to a Maximum Permissible Exposure (MPE) of approximately 1mJ/cm<sup>2</sup>; this falls well below the MPE of skin in the NIR window at that exposure duration of approximately 310mJ/cm<sup>2</sup> [21].

### 2.3.2. K-space re-sampling and point spread function

A phenomenon of increased peak-broadening with increasing path difference was seen in the point spread function (PSF); this is shown in Fig. 3. It was found that since the total approximate length of the fiber laser (as well as the reference arm) before the focusing optics was 23.1m, such a length of fiber introduced a proportional increase in the round-trip time for the photons travelling through the respective arms of the OCT system. For a single trip, this delay was estimated to be:

$$delay = \frac{n(23.1)}{c} = 112ns$$

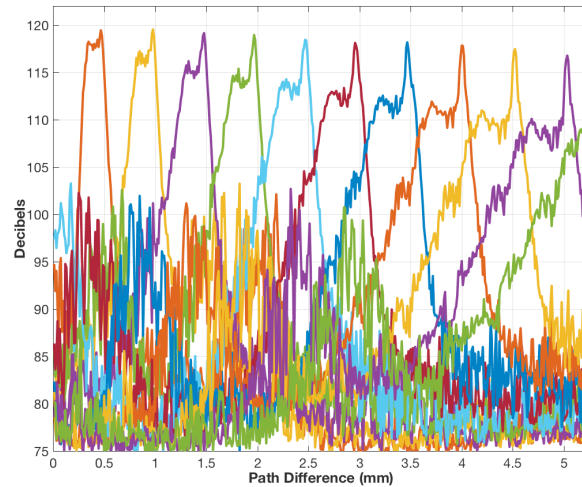


Fig. 3. Point spread function (PSF) of system with no K-clock timing consideration. Optical path difference-dependant peak broadening is very evident due to un-delayed sampling trigger.

where  $n$  is the core refractive index of SMF-28 fiber (1.45205) and  $c$  is the speed of light in vacuum. Therefore, the total estimated increase in round trip time was  $224ns$ . This delay was causing an equal phase shift between the fringe signal from the balanced detector and the k-clock sampling trigger from the swept-source laser, which resulted in incorrectly sampled fringes. To solve this, a Mach-Zender interferometer (MZI) k-space resampling clock was constructed with approximately the same total round-trip optical path length, achieving the same time delay and dispersion. The result of this implementation is shown in Fig. 4. All peaks are seen to be uniformly broadened, which is expected due to dispersion mismatch caused by the sample and reference arms being constructed of mismatched fibers. A  $2^{nd}$  order software dispersion correction algorithm, similar to that found in [22] was used to correct the fixed dispersion mismatch-induced broadening. The resulting PSF is shown in Fig. 5 with corresponding axial resolution values. All PSF measurements were performed by first placing a mirror in the sample arm, then incrementally increasing the path difference between the sample and reference arms. The power in the sample arm was in the mW range, and light from both sample and reference arms were attenuated by free-space apertures to avoid detector saturation.

#### 2.4. A-line triggered ablation pulse synchronization

Figure 6 shows the temporal relationship between the OCT signal acquisition and ablation laser when no synchronization is considered. Reflected leakage light via the fiber combiner was observed to saturate the balanced detector. Although the tilted fiber bragg gratings did attenuate this reflected light so as not to damage the detector, enough optical power did get through to detrimentally affect the A-lines acquired at the same time that the fiber laser emitted output pulses. This was manifested as vertical striping in the OCT image, as shown in Fig. 7. The solution to avoid this problem would be to only fire ablation pulses during the latter half of the A-line period, when no OCT data is being gathered and the swept-source intensity is at its lowest point. A pulse-timing scheme had to be devised such that ablation pulses and A-lines would be time-multiplexed along the same fiber path to avoid laser pulse impingement on A-line data. The new timing scheme, shown in Fig. 8, used the A-line trigger signal generated by the swept-source MEMS laser to trigger the ablation pulses. The TTL-voltage signal was split and sent to a

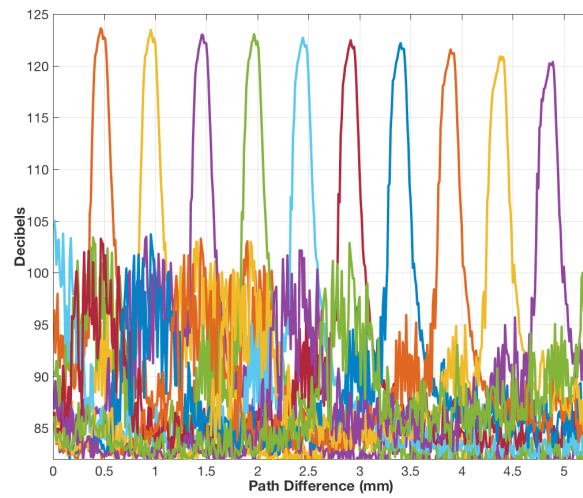


Fig. 4. Point spread function (PSF) of the system with delayed MZI interferometer resampling clock to match round trip time of OCT light. Peak broadening is now approximately uniform due to high dispersion mismatch introduced by the inline fiber laser.

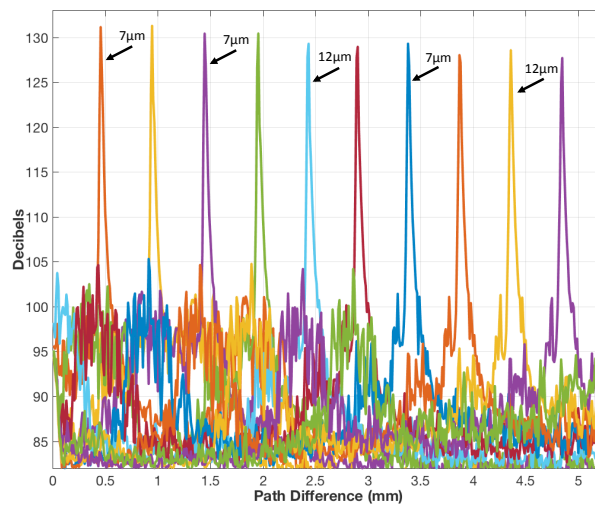


Fig. 5. Point spread function (PSF) of the system with delayed MZI interferometer resampling clock to match round trip time of OCT light and 2<sup>nd</sup> order software dispersion compensation. All axial resolution measurements are full-width, half-Max (FWHM).

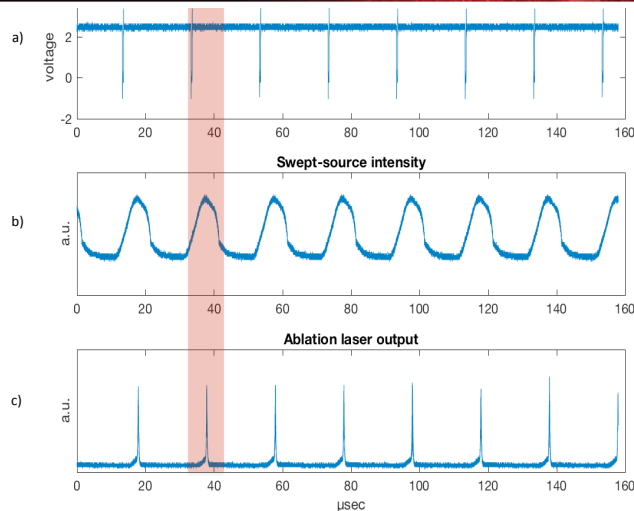


Fig. 6. Timing relation between OCT data acquisition (A-line rate = 50kHz) and ablation laser pulses (50kHz) when no synchronization is implemented (i.e. free-running ablation laser pulsing). The red box highlights which the portion of the cycle where the A-line acquisition takes place. It can be seen from the figure that the ablation pulses (c) clearly impinge on the OCT A-line (after the a-line trigger (a) and during the positive duty-cycle of the swept-source output (b).

function generator (Tektronix AFG3022C) that was programmed to generate a TTL-voltage square pulses  $2\mu\text{s}$  in length and  $8.9\mu\text{s}$  after the rising edge of the A-line trigger. This signal was sent to the external trigger input of the laser diode driver (IXYS Colorado PCX-7420). This timing scheme ensured that the laser pulses would be fired when the OCT system was not acquiring data. The result of this timing scheme is shown in Figs. 9 and 10.

### 2.5. Ablation depth control

Controlled depth ablation experimentation was performed at a laser pulse rate for 50kHz. To control the depth of ablation penetration, the control scheme shown in Fig. 11 was implemented. The in-house developed OCT image processing software was programmed to perform a peak-detection with every incoming A-line to detect the kerf-bottom. The computer was connected via high-speed serial protocol to a microcontroller which had a digital output pin connected to the input of an AND logic gate. The other input of the AND gate was connected to the Tektronix AFG3022C waveform generator, which produced the trigger signal described in the previous section. The output of the AND gate was connected to the external trigger input of the laser diode driver. In this way, the laser diode driver would only receive trigger pulses from the waveform generator if the threshold/target depth had not been reached (i.e. when the microcontroller would output logic 1). Once the depth is reached, the computer would command the microcontroller to output logic 0, therefore not allowing subsequent trigger pulses from reaching the diode driver.

## 3. Experiments and results

### 3.0.1. Phantom drilling

Medium density fiber board (MDF) was used as an ablation phantom due to its material uniformity and its desirable response to thermal ablation at 1064nm. 12 holes were percussion drilled (stationary machining beam relative to workpiece) into the MDF phantom at 5 target depths (0.5mm, 1.0mm, 1.5mm, 2.0mm, 2.5mm), for a total of 60 holes. Depth targeting results are shown in Fig. 12 and summarized in Table 2. The mean depths were measured using b-mode

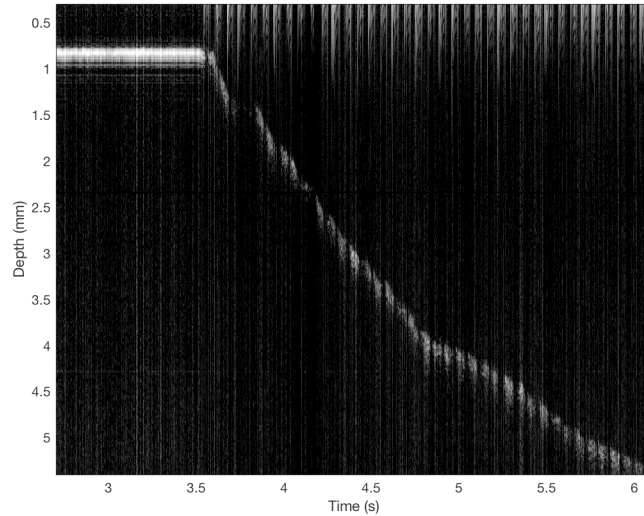


Fig. 7. Depth progression of ablation front during ablation of wood (M-mode). Ablation laser induced artifacts are due to reflected energy through the fiber combiner saturating the balanced detectors.

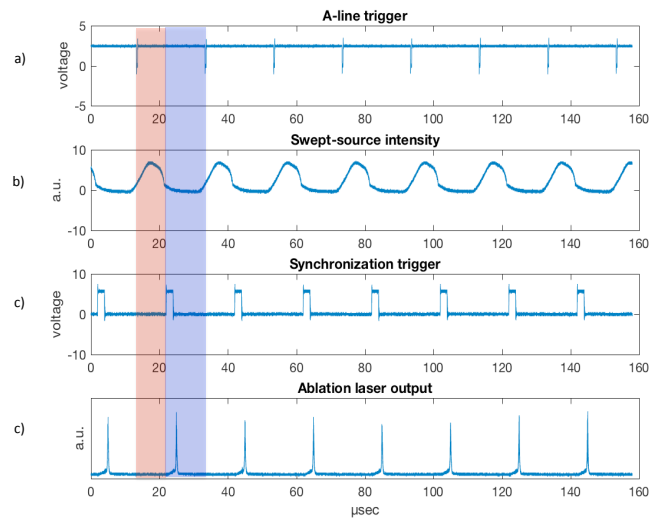


Fig. 8. Timing relation between OCT data acquisition and ablation laser pulses with A-line triggered asymmetric pulse triggering timing scheme implemented. Red and blue boxes highlight portions of the cycle where A-line acquisition occurs and does not occur, respectively. Notice ablation (d) pulses occur only during the latter half of the cycle whilst no A-line acquisition is occurring (i.e. when swept-source output (b) is low). This is due to the fixed timing implemented between laser trigger pulse (c) and the A-line trigger (a).

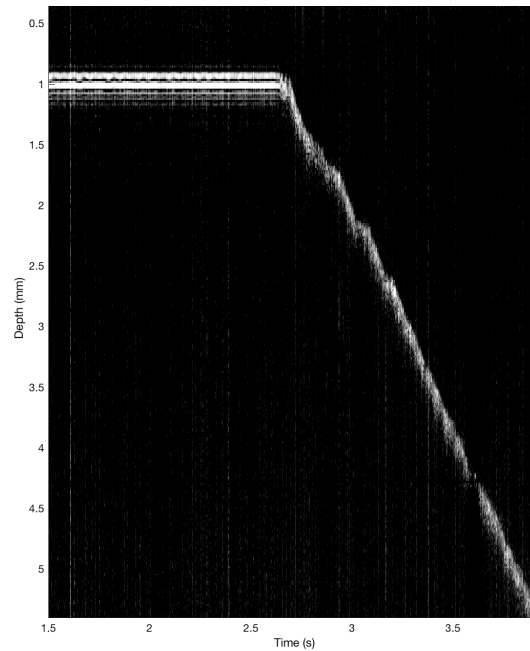


Fig. 9. Depth progression of ablation front during ablation of wood (M-mode) using asymmetric pulse timing scheme. Ablation laser induced artifacts are no longer seen.

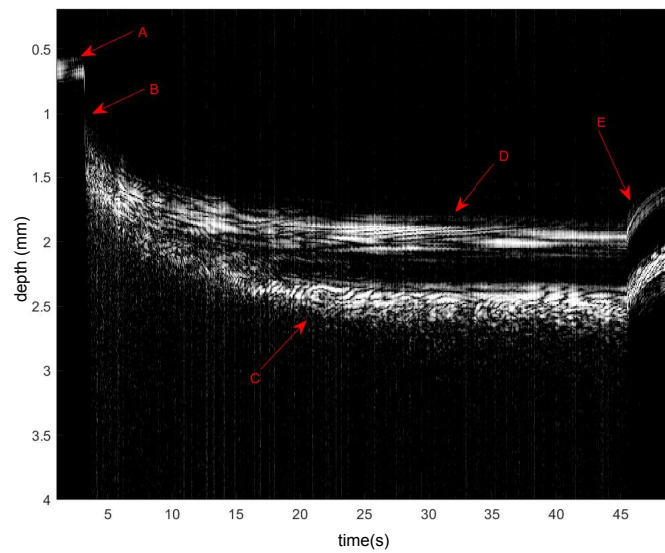


Fig. 10. Depth progression of ablation front during ablative irradiation of fresh porcine scapula (M-mode) using the asymmetric pulse timing scheme described above. A: heating of distal cortical bone surface; B: penetration through cortical layer and center trabecular layer; C: heating of proximal cortical bone layer; D: hole side wall reflection; E: laser shut off, subsequent tissue relaxation/contraction.

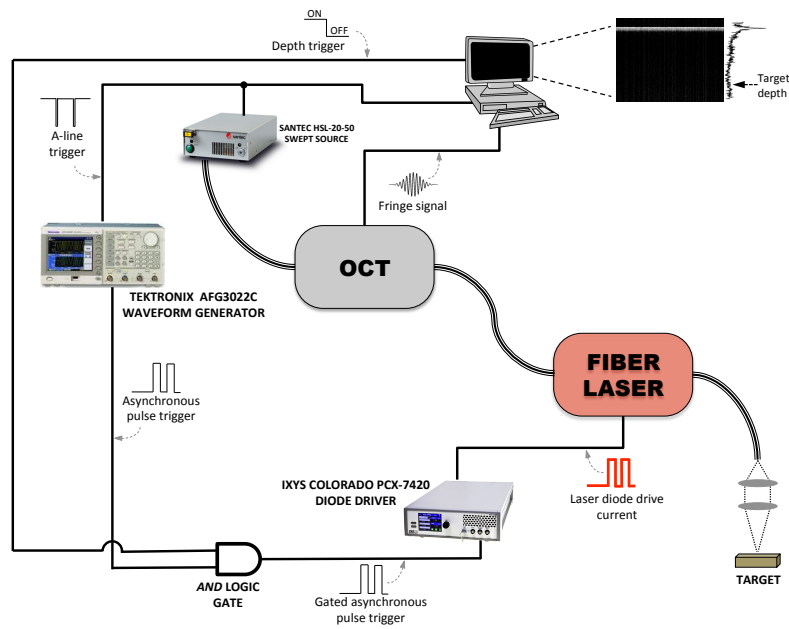


Fig. 11. Diagram of system with integrated depth control. Detection of A-line peak at a target depth triggers a drive-signal shutoff to the ablation laser's pump diode driver.

OCT scans taken using a separate, calibrated, in-house OCT system.

Table 2. Results summarizing drilling depth accuracy experiments on MDF phantom.

Target Depth	Measured Depth	Mean error	Standard Deviation
0.5 mm	0.52 mm	0.020 mm	0.042 mm
1.0 mm	1.01 mm	0.010 mm	0.050 mm
1.5 mm	1.47 mm	-0.030 mm	0.065 mm
2.0 mm	1.957 mm	-0.043 mm	0.051 mm
2.5 mm	2.42 mm	-0.080 mm	0.061 mm

### 3.0.2. Bone drilling

20 holes at two target depths, 0.3mm and 0.5mm, were drilled into the cortical bone of porcine scapula specimens. Table 3 summarizes the measured depth of the bone drilling. The mean depths were measured using b-mode OCT scans taken using a separate, calibrated, in-house OCT system.

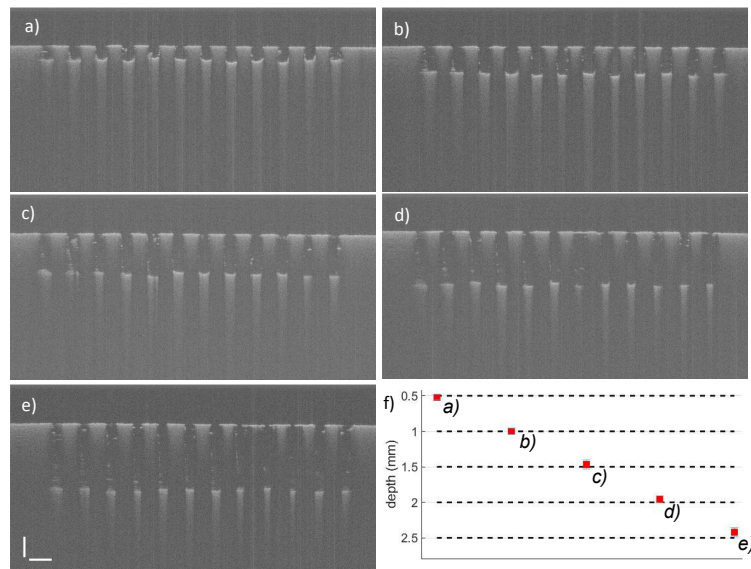


Fig. 12. Ablation depth control trials on MDF phantom. Images a) to e) show OCT scans of the trials starting from 0.5mm target depth to 2.5mm, incrementing by 0.5mm respectively. Scale bars represent 0.5mm. Results are summarized in f). Red squares represent mean measured depths with standard deviation of each panel figure, indicated by the each corresponding label.

Table 3. Results summarizing drilling depth accuracy experiments porcine scapula specimens.

Target Depth	Measured Depth	Mean error	Standard Deviation
0.3 mm	0.306 mm	0.060 mm	0.071 mm
0.5 mm	.0479 mm	-0.021 mm	0.054 mm

#### 4. Discussion and conclusion

We were able to monitor and control the progression of material ablation for wood, MDF and bone for the purposes of real-time metrology and feedback control. The design of this system successfully demonstrated feasibility of integrating a high power fiber laser into the sample arm of a standard swept source OCT system and allowing coaxial ablation monitoring and control. This type of laser topology can be applied to both medical and non-medical ablation applications. We measured the bending loss through the SM-GDF-10/125, which contribute to the decreased SNR of OCT imaging. We were also able to show that dispersion and light propagation delay does in fact occur due to the addition of the fiber laser in the sample arm of the OCT system.

This design provides some unique advantages over existing designs that employ a dichroic mirror for beam coupling. The removal of the dichroic mirror means that the objective stage of the system can be made extremely compact because only a collimator and focusing lens is required (for M-mode capability) for full ablation and tracking capabilities. Coaxial beam alignment happens by virtue of fiber coupling and therefore does not require free-space optics and multi-DOF kinematic mounts. As well, the system has great potential to be miniaturized due to the all-fiber design in the sample arm. The two largest components of the entire system are the Santec HSL-20-50 swept source (194x135x53mm) and the RealLight M976±3-110-F105/22-D1

pump diode (85x58x20mm). There is no need for active cooling in any part of the system; passive heat sinking is sufficient to carry away residual heat from the pump diode package. Since the rest of the system is constructed of fiber based components, the potential packaging volume could be no larger than the size of a laptop computer or textbook. This potential form factor makes this design uniquely attractive for surgical applications.

This design does have some potential drawbacks. First, the fiber laser does seem to be highly dispersive to the OCT sample beam. Dispersion compensation, optically or algorithmically, needs to be done in order to ensure optimal system performance; we have demonstrated a solution to this. Also, attenuation of OCT light due to the large mode area fiber of the ablation laser does degrade OCT fringe quality. We have demonstrated that an optical amplifier can be used to increase the incident swept-source power, but the backscatter travelling from the sample and back through the system is subject to the high attenuation. However, since the surface of the ablation kerf is the main feature of concern, this system can still prove to be extremely useful in surgical settings given its potential for compactness. Also, to mitigate bending losses during surgery, an inexpensive armoured sheath can be used to encase the output fiber to limit the bend radius to greater than approximately 60mm. Armoured optical cables such as this are already in ubiquitous use in many industrial and medical applications that require any sort of critical optical fiber outside of an enclosure to be protected from mechanical and chemical damage.

As well, we attribute the targeting error being larger than the resolution system because the control loop is potentially slower than the pulse rate of the ablation laser. Speeding up the loop rate could demonstrate greater targeting accuracy, however the reported targeting accuracy in this manuscript well surpasses the suitability for bone drilling (given that the current paradigm involving hand drilling by surgeons can not necessarily achieve such precision). As well, the inclusion of faster electronics to speed-up the control loop frequency could potentially increase system cost and communication scheme complexity. Potential limitations of the peak detection algorithm could include system response to spurious reflections as peaks, as well as potentially decreasing visibility of the peak as ablation progresses and carbonization becomes the dominant absorber.

Using this novel topology, we were able to demonstrate top-down feedback, meaning distance of penetration measured from the top of the sample to the bottom of the kerf. This integrated system has the potential to visualize sub-surface interfaces well before penetration by the ablation front. By doing this, a bottom-up feedback system (measured up from the subsurface interface) could be used to control penetration of the laser with little to no *a priori* knowledge of the material being ablated. Further applications of interest are to mount the output optics onto electro-mechanical motion systems (galvanometer driven mirrors, multi-DOF robotic systems) and use the OCT depth feedback for motion control (i.e. hover time, feed rate and continuous focusing of kerf floor).

## Funding

Natural Sciences and Engineering Research Council of Canada; The Canada Foundation for Innovation.

## Disclosures

The authors declare that there are no conflicts of interest related to this article.

## References

1. W. Steen, K. G. Watkins, and J. Mazumder, *Laser Material Processing* (Springer Science and Business Media, 2010).
2. L. A. Kahrs, J. Burgner, T. Klenzner, J. Raczowsky, J. Schipper, and H. Wörn, "Planning and simulation of microsurgical laser bone ablation," *Int. J. Comput. assisted radiology surgery* **5**, 155–162 (2010).
3. S. Stopp, D. Svejdar, E. Von Kienlin, H. Deppe, and T. C. Lueth, "A new approach for creating defined geometries by navigated laser ablation based on volumetric 3D data," *Biomed. Eng. IEEE Transactions on* **55**, 1872–1880 (2008).

4. L. A. Kahrs, J. Raczkowsky, M. Werner, F. B. Knapp, M. Mehrwald, P. Hering, J. Schipper, T. Klenzner, and H. Wörn, "Visual servoing of a laser ablation based cochleostomy," in *Visual servoing of a laser ablation based cochleostomy*, (International Society for Optics and Photonics, 2008), pp. 69182C.
5. S. A. Boppart, J. Herrmann, C. Pitris, D. L. Stamper, M. E. Brezinski, and J. G. Fujimoto, "High-resolution optical coherence tomography-guided laser ablation of surgical tissue," *J. Surg. Res.* **82**, 275–284 (1999).
6. S. A. Boppart, J. M. Herrmann, C. Pitris, D. L. Stamper, M. E. Brezinski, and J. G. Fujimoto, "Real-time optical coherence tomography for minimally invasive imaging of prostate ablation," *Comput. Aided Surg.* **6**, 94–103 (2001).
7. M. Ohmi, M. Tanizawa, A. Fukunaga, and M. Haruna, "In-situ observation of tissue laser ablation using optical coherence tomography," *Opt. Quantum Electron.* **37**, 1175–1183 (2005).
8. W. Oh, S. Yun, B. Vakoc, G. Tearney, and B. Bouma, "Ultrahigh-speed optical frequency domain imaging and application to laser ablation monitoring," *Appl. Phys. Lett.* **88**, 103902- (2006).
9. M. Ohnishi, D. Takada, M. Ohmi, and M. Haruna, "Dynamic analysis of laser ablation of biological tissue using a real-time OCT," *Measurement Science and Technology* **21**(9), 717513 (2009).
10. M. Ohmi, M. Ohnishi, D. Takada, and M. Haruna, "Real-time OCT imaging of laser ablation of biological tissue," *Proc. SPIE* **7562**, 756210 (2010).
11. B. A. Torkian, S. Guo, A. W. Jahng, L.-H. L. Liaw, Z. Chen, and B. J. Wong, "Noninvasive measurement of ablation crater size and thermal injury after co2 laser in the vocal cord with optical coherence tomography," *Otolaryngol. Neck Surg.* **134**, 86–91 (2006).
12. P. J. Webster, M. S. Muller, and J. M. Fraser, "High speed in situ depth profiling of ultrafast micromachining," *Opt. Express* **15**, 14967–14972 (2007).
13. P. J. Webster, B. Y. Leung, X. Joe, M. D. Anderson, T. P. Hoult, and J. M. Fraser, "Coaxial real-time metrology and gas assisted laser micromachining: process development, stochastic behavior, and feedback control," in *MOEMS-MEMS*, (International Society for Optics and Photonics, 2010), pp. 759003.
14. B. Y. Leung, P. J. Webster, J. M. Fraser, and V. X. Yang, "Real-time guidance of thermal and ultrashort pulsed laser ablation in hard tissue using inline coherent imaging," *Lasers Surg. Medicine* **44**, 249–256 (2012).
15. K. Beaudette, H. W. Baac, W.-J. Madore, M. Villiger, N. Godbout, B. E. Bouma, and C. Boudoux, "Laser tissue coagulation and concurrent optical coherence tomography through a double-clad fiber coupler," *Biomed. Opt. Express* **6**, 1293–1303 (2015).
16. K. Beaudette, W. Lo, M. Villiger, M. Shishkov, N. Godbout, B. E. Bouma, and C. Boudoux, "Towards in vivo laser coagulation and concurrent optical coherence tomography through double-clad fiber devices," in *Multimodal Biomedical Imaging XI*, volume 9701 (International Society for Optics and Photonics, 2016), p. 97010B.
17. J.-L. Boulnois, "Photophysical processes in recent medical laser developments: a review," *Lasers Med. Sci.* **1**, 47–66 (1986).
18. J. Jivraj, Y. Huang, R. Wong, Y. Lu, B. Vuong, J. Ramjist, X. Gu, and V. Yang, "Coaxial cavity injected oct and fiber laser ablation system for real-time monitoring of ablative processes," in *Proc. SPIE BiOS*, (2015), pp. 930505.
19. J. Jivraj, J. Zhou, X. J. Gu, and V. X. Yang, "Coaxial cavity injected oct and fiber laser ablation system for real-time monitoring of ablative processes part 2: toward all fiber design and dispersion control," *Conference Presentation* (2017).
20. Y. Lu and X. Gu, "All-fiber passively q-switched fiber laser with a sm-doped fiber saturable absorber," *Opt. express* **21**, 1997–2002 (2013).
21. A. N. S. I. Standard, *Z136. 1–2007* (American National Standard for the Safe Use of Lasers, 2007).
22. M. Wojtkowski, V. Srinivasan, T. Ko, J. Fujimoto, A. Kowalczyk, and J. Duker, "Ultrahigh-resolution, high-speed, Fourier domain optical coherence tomography and methods for dispersion compensation," *Opt. Express* **12**, 2404–2422 (2004).